The Journal of Chemical Physics

RESEARCH ARTICLE | JULY 11 2025

Multi-mode water dynamics in hydration shells of villin headpiece subdomain protein in the solid state using deuterium and oxygen-17 NMR spectroscopy

Liliya Vugmeyster ; Bailey Frazier; Riqiang Fu ; Dmitry Ostrovsky

J. Chem. Phys. 163, 025101 (2025)
https://doi.org/10.1063/5.0279081
CHORUS

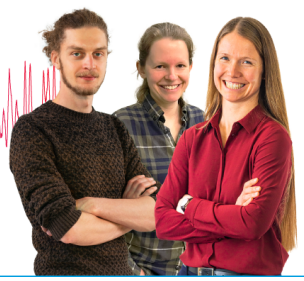

AIP Publishing

The Journal of Chemical Physics ARTICLE pubs.aip.org/aip/jcp

Multi-mode water dynamics in hydration shells of villin headpiece subdomain protein in the solid state using deuterium and oxygen-17 NMR spectroscopy

Cite as: J. Chem. Phys. 163, 025101 (2025); doi: 10.1063/5.0279081
Submitted: 5 May 2025 • Accepted: 20 June 2025 •
Published Online: 11 July 2025

Liliya Vugmeyster,[1,a)] Bailey Frazier,[1] Riqiang Fu,[2] and Dmitry Ostrovsky[3]

AFFILIATIONS

[1] Department of Chemistry, University of Colorado at Denver, Denver, Colorado 80204, USA
[2] National High Magnetic Field Laboratory, Tallahassee, Florida 32310, USA
[3] Department of Mathematical and Statistical Sciences, University of Colorado at Denver, Denver, Colorado 80204, USA

[a)] **Author to whom correspondence should be addressed:** liliya.vugmeyster@ucdenver.edu

ABSTRACT

Hydration shell properties in proteins remain an active topic of investigation due to their complexity and importance for biological processes. We focused on hydration shell dynamics in the solid state of the globular villin headpiece subdomain (HP36). We utilized ^{2}H (D_2O hydration) and ^{17}O ($H_2{}^{17}O$ hydration) solid-state NMR spectroscopy in combination with computational modeling to obtain a comprehensive picture of water motions, starting from high-amplitude modes such as diffusion and large-angle tetrahedral jumps and progressing to lower-amplitude modes such as 2-site deuteron flips and small-angle fluctuations. The measurements consisted of NMR line shapes as well as laboratory and rotating frame relaxation rates using novel approaches, conducted in the 300–170 K temperature range and at multiple values of magnetic field strengths. They permitted the precise determination of motional parameters such as fractions of different water layers, rate constants, and activation energies. Below about 250 K, both ^{2}H and ^{17}O longitudinal relaxation show clear non-exponential behaviors, with at least two components whose T_1 times differ by orders of magnitude. The water layer immediately adjacent to the protein surface remains mobile, as probed by the hydration dependence of NMR relaxation in the 20%–70% w/w water content range. Further, the observed non-exponentiality of ^{17}O $T_{1\rho}$ relaxation at low temperatures suggests an exchange process between the layer adjacent to the protein and loosely bound shells. Based on prior results, we discuss correlations with dynamical changes in the hydrophobic core of HP36, thus obtaining insights into the interconnection of protein and water dynamics.

I. INTRODUCTION

A. Importance of hydration layers for biological function

The importance of hydration layers of proteins for multiple biological functions has been recognized for many decades, in topics such as protein folding/misfolding, molecular recognition, ion channel selectivity and gating, enzymatic catalysis, and others.[1–5] The topic constantly gets revisited and knowledge updated due to the complexity of water and ice behavior at interfaces and the paramount importance of water for biological life and biomolecular functioning. The dynamical behavior of water in solutions[6,7] and in hydrated protein powders[8–10] has been studied extensively both experimentally and computationally.[11–14]

The definition of hydration shells differs in the literature.[6,15,16] While intuitively it is clear that water confinement, surface interactions, and hydrogen-bonding pattern distortions in the presence of a protein surface change the arrangement of the water molecule network and its dynamics, the precise boundary where the "bulk" water layer ends and the water behavior changes from its bulk state is not clearly defined. In fact, it can be somewhat dependent on the method of investigation. The fuzziness of the definitions between the

relatively free and bound/confined water layers may be even starker in the case of concentrated protein systems, hydrated crystals, or hydrated protein powders.[17,18] Further, a number of studies suggested that the layer immediately adjacent to the protein surface can retain substantial mobility down to low temperatures.[19–21]

The dynamics of hydration shells and those of the protein itself are coupled,[22] and multiple works have characterized the effect of water on the so-called protein dynamical (second-order) and glass transitions.[23–30] These phenomena appear to occur in stages from about 260 down to 120 K.[29–33] The ranges are loosely defined in the literature and are rather dependent on the observation window dictated by specific spectroscopic techniques, such as x-ray diffraction, neutron scattering, dielectric spectroscopy, IR, and NMR relaxation. The freezing of large-amplitude and anharmonic modes is believed to be strongly coupled to the properties of the water network, especially the shells in immediate proximity to the protein. Hydrogen bonding network activation, of both the protein and adjacent hydration shell, is expected to occur at around 170 K.[23,29,33,34] The freezing of collective protein modes and anharmonic fluctuations is often associated with the loss of biological activity.[23,25] In turn, the influence of protein properties on water dynamics has also been extensively considered in the literature, with factors such as water confinement, surface polarity, hydrogen bonding, and flexibility considered in detail.[15,22]

B. The system

In this work, we investigate water behavior in the hydrated powder state of a well-studied small globular protein, the villin headpiece subdomain protein (HP36).[35] Villin is an F-actin bundling protein involved in the maintenance of the microvilli of the absorptive epithelia.[36] The villin headpiece subdomain is a 35-residue, autonomously folding, thermostable motif at the extreme C-terminus of villin.[35] This subdomain spans residues 42–76 (residues 791–825 of intact chicken villin) of the full-length villin headpiece. The recombinant form of the subdomain, HP36, has an additional N-terminal methionine residue designated arbitrarily as residue 41. The structure of HP36, as determined by x-ray and NMR spectroscopy,[37,38] consists of three short helices surrounding a tightly packed hydrophobic core [Fig. 1(a) and Fig. S1 of the supplementary material]. F47, F51, and F58 form the basis of the core, flanked by the methyl groups of V50, L61, and L69.

When working with the hydrated powder state of globular proteins, the level of hydration is one of the important factors that can influence the dynamics of both the protein itself and the hydration shell. In general, it has been found that a hydration level of about 20% by mass (w/w) is needed to retain native-like behavior of the proteins, and many works employ hydration levels in the range of 35%–40%, with some studies raising this level to 60%–80%.[34] Raising the level even higher beyond 70%–80% creates a significant predisposition toward partially dissolving the protein. In this work, we use the maximum hydration level of 70% w/w but also probe selected features of water dynamics at lower hydration levels of 20% and 40%.

C. Methods overview

Hydration water properties have been assessed by a number of experimental techniques, including x-ray diffraction and neutron scattering, dielectric spectroscopy, NMR and NMR relaxometry, IR, two-dimensional IR spectroscopy, terahertz, Raman methods, and others.[15] Most of the studies cannot distinguish between individual water molecules, although specific techniques in solid-state NMR can identify selected tightly bound water molecules attached to the protein surface.[2,39,40] Tightly bound water molecules can also be observed in crystallographic[41,42] or cryo-EM protein structures.[43] Spatially heterogeneous water dynamics has been observed in solution with the use of Overhauser dynamic nuclear polarization[17,44] or by reverse micelle encapsulation in combination with solution NMR.[45]

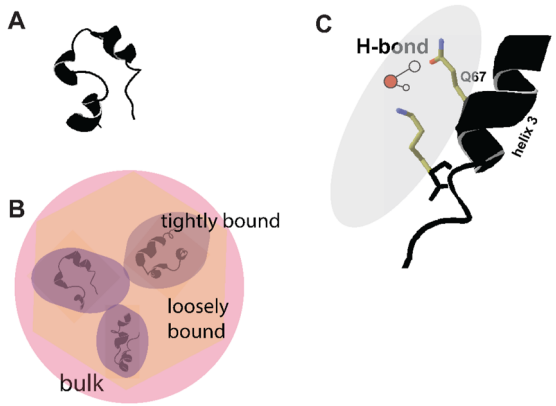

FIG. 1. (a) Ribbon diagram of HP36 protein, PDB ID 1YRF.[37] (b) A schematic diagram of the hydrated powder state indicating bulk, loosely bound/intermediate, and tightly bound water layers. (c) The tightly bound water layer immediately adjacent to the protein surface, shown schematically for the expansion of the 63–76 amino acid region of HP36 (spanning helix 3 and the C-terminal tail): hydrogen bonding of a water molecule to the side-chain carbonyl oxygen of GLN67 residue is shown as an example.

The spectroscopic methods employed in this work, deuterium and oxygen-17 solid-state NMR, have long been recognized as important, sensitive tools for studies of water dynamics in the solid and colloidal states in a variety of organic,[46–48] inorganic,[49–53] and biological materials[54,55] and proteins,[13,20,55–60] as well as in pure ice.[61–63] For both nuclei, the main interaction governing spectroscopic properties is the quadrupolar interaction, which is the interaction between the nuclear spin with the spin number greater than 1/2 and the electric field gradient, caused by an asymmetric distribution of electron density around the nucleus.[64] Deuterium has a spin of 1, and oxygen-17 that of 5/2. Without accounting for motions, the quadrupolar interaction constant (C_q) of deuterons in frozen hydration shells and ice spans about the 200–260 kHz range, while that of ^{17}O is on the order of 6.5–9 MHz.[65,66] Distortions in quadrupolar NMR line shapes induced by motions can be used to quantify the mechanisms and timescales of motions.[46,49,67,68] In addition, relaxation measurements can provide useful complementary information on a variety of timescales.[46,69–71] It is well known that covering multiple types of NMR measurements and including a broad temperature range and field dependence permits the most precise determination of motional mechanisms and motion parameters.

We have recently conducted a detailed combined analysis of ^{17}O CT line shapes, rotating frame ($T_{1\rho}$), transverse (T_2),

and longitudinal (T_1) relaxation times in ^{17}O enriched sodium nitrate under static (non-spinning) conditions, supplemented by simulations using the numerical integration of the Liouville–von Neumann equation.[70] Recently, Dai *et al.* also used T_2 of the satellite transitions to study dynamics in sodium nitrite.[72] We expand the ^{17}O CT methodological approach to studies of much more complicated systems, that is, water in hydrated protein shells. In the presence of multiple modes of motion, relevant to the water molecules in the protein environment, different experiments allow for the disambiguation of these modes and the determination of their rate constants due to different sensitivities of the experiments to the geometries and rates of motion. The experimental methodology is expanded by also incorporating filtering blocks that permit the differential detection of mobile and rigid water fractions.[73]

D. Goals of this work

The question that we pose is what are the main motional modes of water in mobile and motionally restricted hydration layers of HP36, as probed in the broad temperature range of ~300 to 170 K. Based on detailed solid-state NMR data taken at several static magnetic field strengths, we devise a framework of these modes, starting with large-angle, nearly isotropic fluctuations at high temperatures and moving to smaller-angle motions as the mobility decreases with temperature. Intriguing dynamical features are observed for the layer directly in contact with the protein surface, which retains high mobility down to low temperatures, with the onset of the separation of the dynamics of the layers at 250 K. We also observe the exchange between the layer in closest proximity to the protein and those at a further distance from the protein surface. The experiments probing different hydration levels are conducted to arrive at these conclusions. Based on prior results of ring-flip activation barriers in the core phenylalanine groups[74] as well as the rate constants and activation barriers for rotameric jumps of key methyl groups,[75] we observe correlations between hydration layers' dynamics and the hydration dependence of the protein dynamical modes.

II. MATERIALS AND METHODS

A. Sample preparation

HP36 peptide was synthesized commercially using solid-phase peptide synthesis (Life Sciences Corporation) and purified to at least 95% purity. The primary sequence of HP36 is MLSDEDFKAVFGMTRSAFANLPLWKQQNLKKEKGLF. HP36 was dissolved in Milli-Q purified water, and its pH was adjusted to 6, then lyophilized before rehydration. The lyophilized protein powder was rehydrated with either 99% D_2O or 70% enriched $H_2{}^{17}O$ for NMR studies by pipetting the required amount of water and mixing inside the NMR container. The samples were equilibrated for at least 48 hours after mixing and underwent two freezing–thawing cycles, including flash-freezing in liquid nitrogen to ensure the most homogeneous hydration. The NMR containers were custom-made 5-mm-diameter tubes with the capacity to seal liquid using caps with O-rings. The water content varied between 0.2 and 0.7 μl of water per 1 mg of protein.

B. NMR spectroscopy

1. Static line shapes

For ^{2}H nuclei, the quadrupolar echo (QE) scheme was used.[69] A QE delay between 25 and 31 μs was employed to minimize acoustic ringing. The excitation 90° pulse was 2 μs, ensuring adequate excitation of the full powder pattern. ^{2}H longitudinal relaxation times for the rigid components, as described in Sec. III, can exceed 500 s at low temperatures. Thus, a long recycle delay was needed, resulting in a relatively low number of scans collected.

For ^{17}O nuclei, either the traditional Hahn echo scheme[76] or the TRIP sequence[77] was employed to minimize acoustic ringing. The echo scheme reduces signal intensity due to T_2 losses. Therefore, at higher temperatures, where T_2 relaxation is fast, the TRIP collection scheme was used for ^{17}O nuclei.

An essential feature of the TRIP sequence is its ability to act as a selectivity filter depending on the extent of motional averaging of C_q: to excite mobile states with effective C_q~0, one employs a series of an odd number of 60° pulses with the appropriate phase cycling scheme.[73,77] A larger number of pulses increases the level of selectivity at the expense of signal suppression. To selectively excite the rigid states with $C_q \gg \omega_1/2\pi$, a series of 30° pulses is used instead. The RF field strength, $\omega_1/2\pi$, employed for excitation was 41.7 kHz.

At temperatures below 200 K, distortions were visible when using the TRIP scheme due to receiver dead time issues; therefore, the Hahn echo scheme was employed with a 25 μs echo delay. If pure excitation of the CT transition is desired, the excitation pulse must be selective enough to exclude all crystallites of the first satellite transition. Alternatively, a saturated state of the ST1 can be achieved using selective off-resonance irradiation centered at the ST1. We used a sequence consisting of ten pairs of Gaussian pulses of 10 μs duration with ±300 kHz offset, spaced at 1 μs intervals, referred to as the "RAPT block." This block is an extension of the prior scheme by Haase *et al.*[78] TPPM decoupling of protons[79,80] using 80 kHz RF field strength was employed during acquisition.

2. Relaxation time measurements

^{2}H T_1 relaxation time measurements were performed using the inversion or saturation recovery sequences with the QE detection scheme.[69] ^{17}O T_1 measurements for the mobile (free) fraction with effective C_q values close to zero were performed using the inversion recovery sequence, without pre-saturation of ST1 but using the 3-pulse TRIP excitation filter as described in Sec. II A. T_1 measurements for layers with more restricted motions (i.e., those with large quadrupolar coupling constants given by the condition $C_q \gg \omega_1/2\pi$) were performed as follows: (a) with the inversion recovery sequence using the 7-pulse TRIP filter for T_1 values below 100–200 ms. For the temperatures at which a significant free fraction remained, additional suppression was invoked using a T_1-flittering delay of $T_1^{free}\ln(2)$, similar to the approach used by Zhang *et al.*;[73] (b) for T_1 times longer than about 200 ms, the saturation recovery scheme was used, preceded by the RAPT pre-saturation of ST1 and using either the 3-pulse or 7-pulse TRIP filter as the detection block.

The pulse sequence for the ^{2}H static $T_{1\rho}$ measurements is described in detail in Ref. 71. The spin-locking field of 41 kHz was employed. ^{17}O $T_{1\rho}$ measurements incorporated a variation of the

pulse scheme described in Ref. 70, with the insertion of a heat compensation block[81] and the TRIP-based selective excitation (Fig. S2 of the supplementary material). After the heat compensation block, the RAPT suppression of ST1 coherences was employed, followed by the TRIP scheme excitation, and then the spin-lock period of variable delay, applied at the center of the spectrum (on-resonance) with the RF field amplitude of 35 kHz. The 3-pulse TRIP filter with 60° excitation pulses was used to excite signal from the mobile (bulk and loosely bound) states of water. For the tightly bound state, similar to T_1 collection, the 7-pulse TRIP scheme with an additional T_1-filtering delay was used at higher temperatures with a significant fraction of the mobile state, while at lower temperatures, the 3-pulse TRIP block was employed without the additional filtering. TPPM decoupling of protons using 80 kHz RF field strength was employed during acquisition, while at lower temperatures continuous-wave (cw) decoupling with a 70 kHz RF field strength was also employed during the rotating frame relaxation period, as discussed in Sec. III. For temperatures below 180 K, due to long relaxation times of the slowly relaxing component (60 s at 180 K and 18.8 T), the interscan delay was cut to 35%–50% of T_1 time value, and the number of dummy scans was increased to 16 from the value of 8 used at higher temperatures. At temperatures above 180 K, the interscan delay was at least $1.5 \cdot T_1$. T_2 relaxation times in the 220–180 K temperature range were collected at 18.8 T field strength using the Hahn echo pulse sequence with SPINAL64 decoupling[82] during the relaxation period. Other pulse sequence blocks involved in T_2 relaxation time measurements, such as 3-pulse TRIP and RAPT filters, were analogous to those used for $T_{1\rho}$ times.

3. Data processing

^{2}H spectra were processed with 0.5 kHz Lorentzian line broadening above the temperatures at which significant spectral broadening onset is observed (around 250 K), and with 1 kHz line broadening below this temperature. The spectra were centered. ^{17}O spectra were processed with 1 kHz line broadening and referenced to the natural abundance ^{17}O signal of tap water at 280 K.

The same window function parameters were used in the processing of the relaxation data. The magnetization build-up and decay curves were constructed using integration over the entire powder pattern spectra. Mono-exponential T_1 inversion and saturation magnetization recovery curves, as well as mono-exponential $T_{1\rho}$ magnetization decay curves, were fitted to the function $M(t) = M_\infty + (M_0 - M_\infty)e^{-t/T}$. The non-exponential decays were fitted with Eq. (1), as described in Sec. III.

C. Computational approaches

Simulations of ^{17}O and ^{2}H line shapes and relaxation decay/build-up curves were performed as described in prior works.[70,71,83,84] Inclusion of the Liouvillian approach is important for the rotating frame relaxation, which is based on numerical integration of the Liouville–von Neumann equations by matrix exponentiation using an internal MATLAB algorithm. For the relaxation data, magnetization decay and build-up curves were simulated with the same delay times used in the experiments.

Motional modeling is based on the multi-frame approach developed by Vold and Hoatson,[83] involving nested frames when multiple motional modes are involved. While two- or three-site jump simulations for the 2-site deuteron flips or tetrahedral jumps are straightforward, inclusion of diffusion for the case of a highly anisotropic ^{17}O EFG tensor requires a grid with precise coverage of rotations along all three axes. We used a scheme based on 60 orientations derived from the 600-cell in a space of unit quaternions.[85] The Euler's angles, matrices of rate constants, and other approaches used for individual motional modes are shown in supplementary material SI1 along with the powder averaging parameters.

1. Error analysis

The errors in the fitted values of the model parameters resulting from the relaxation data were in general obtained by the inverse correlation matrix method,[86] while fitting the simulated magnetization decay curves to their corresponding theoretical expressions. For fits involving ^{2}H T_1 and $T_{1\rho}$ data at temperatures higher than 250 K, diffusion and the 2-site flip modes were used jointly. In this case, the errors in the fitted parameters were obtained based only on the experiment to which a particular mode is most sensitive, T_1 times for the flip mode and $T_{1\rho}$ times for the diffusion mode. The errors in the parameters obtained via solving McConnell equations for low-temperature ^{17}O $T_{1\rho}$ relaxation—most notably the exchange rate constants—were propagated using equations given in the supplementary material SI1.

III. RESULTS AND DISCUSSION

NMR measurements were performed under static (non-spinning) conditions. The general temperature range spanned 300–170 K, and some of the relaxation measurements, as detailed below, were measured at several magnetic field strengths of 9.4, 14.1, and 18.8 T. ^{17}O NMR probed specifically the central transition (CT) of the ^{17}O spin 5/2 system. The main results are presented for HP36 protein hydrated to the 70% w/w hydration level. Additional data for different levels of hydration are presented for studies at lower temperatures, geared toward deciphering the dynamics of the layer immediately adjacent to the protein surface. As detailed in Sec. II A, the hydration was performed with either D_2O or $H_2{}^{17}O$, with isotopic enrichment levels of 99% and 70%, respectively.

The bulk freezing point of D_2O is 277 K, but for rehydrated protein powders it is in the 273–268 K range. In comparisons of all ^{2}H and ^{17}O NMR data results, we do not make the correction for the higher bulk freezing point of pure D_2O vs H_2O, as within the uncertainties of the measurements these are less important than the effect of protein powder environments themselves.

Fitting multiple motional modes present in several hydration layers cannot be done without qualitative understanding of the characteristics of the experimental data. Therefore, we postpone the detailed analysis of the motional modes until the experimental data are presented.

A. ^{2}H and ^{17}O temperature dependent line shapes

1. Overview of the experimental line shape data

Figure 2(a) shows ^{2}H static line shapes. At 302 K, a narrow line is observed with a width at half-height of about 2.3 kHz. The line shape narrowing indicates that all hydration shells have motions in the fast motional regime. At the intermediate temperature range of

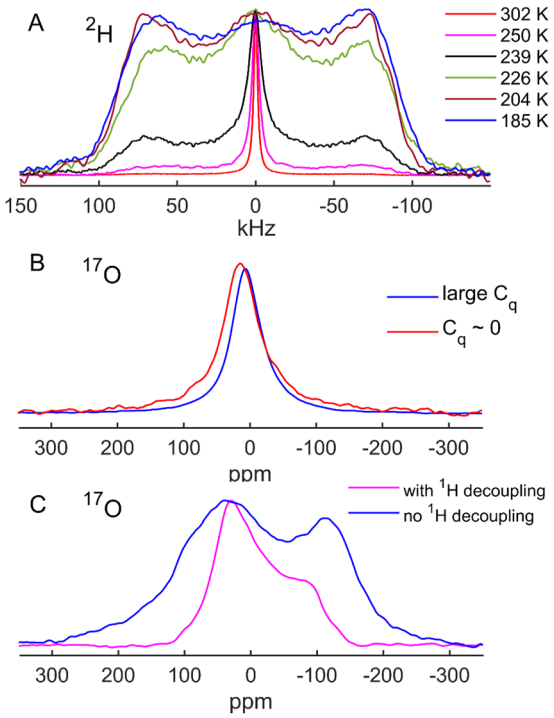

FIG. 2. Examples of normalized solid-state NMR line shapes of water in the hydration shells of HP36 protein, with water content of 70% w/w. The data were collected under static (non-spinning) conditions. (a) ^{2}H line shapes collected using the QE scheme[69] at 9.4 T magnetic field strength at different temperatures, shown directly on the panels. (b) ^{17}O CT line shapes at 18.8 T and 260 K for the states of water with large C_q (blue line) and those with small C_q (red line), selected using the 7-pulse TRIP filter.[73,77] The relative intensities are adjusted according to the appropriate TRIP scaling factors. Referencing is performed to the chemical shift of ^{17}O nuclei in tap water at 280 K. (c) ^{17}O CT line shape at 180 K and 18.8 T using the 3-pulse TRIP filter and either including (magenta line) or omitting (blue line) proton TPPM decoupling[80] during acquisition.

250 to about 220 K, it is apparent that the deuteron line shapes are a combination of narrow and wide patterns, implying a mixture of different mobilities of water layers.

For the ^{17}O-based measurements, a selectivity filter was used that permits selection of either the highly mobile states with the effective quadrupolar coupling constant averaged to about zero (referred to as "small C_q" below), or more rigid states with the quadrupolar coupling constant much greater than the RF irradiation employed to excite it (referred to as "large C_q"). The selection is based on the differences in their nutation frequencies. The selection is achieved using the so-called "TRIP" block and additional filtering, as detailed in Refs. 73 and 77 and in Sec. II. The ^{17}O line shapes of more rigid layers [Fig. 2(b)] also display an overall widening, which in this case is not only due to motional freezing but also due to the effects of coherent dipolar coupling interaction with protons. At high temperatures, proton flips, discussed in detail below, cause an effective decoupling of the dipolar H–O interactions. At lower temperatures, proton decoupling schemes must be incorporated to remove at least the heterogeneous proton–oxygen dipolar effects.

2. Determination of the relative fractions of mobile and rigid states based on the line shapes

Throughout this work, we will employ the definition of hydration shells illustrated in Fig. 1(b): the bulk layers furthest away from the protein surface, the tightly bound layers closest to the protein surface, and the loosely bound/intermediate layers spanning the continuum from the bulk to the tightly bound layers. It is not immediately clear how these layers contribute to the individual features of the line shape and the relaxation data, and our analysis provides suggestions based on all combined results and knowledge from the literature as to how to interpret the experimental data in terms of contributions from different water layers.

^{2}H line shape data can be decomposed into the relatively narrow Lorentzian and wide components in the range of 250–220 K, the former corresponding to the mobile "free" fraction (p_{free}), and the latter to contributions from the more rigid layers, with details of decomposition and the error analysis shown in Fig. S3 of the supplementary material. The narrow component itself has two contributions from a very narrow Lorentzian line (2.3 kHz width at half-height), most likely representing the remaining unfrozen bulk water, and an additional wider Lorentzian shape, representing the mobile state of all layers undergoing symmetrical motions. The wide fraction represents frozen layers, as well as remaining mobile layers that undergo anisotropic motions and do not lead to effective line shape averaging. The resulting values of p_{free} are shown in Fig. 3 in circles. Above about 250 K, the contribution of the less mobile fraction is not visible within the level of the noise and residual distortions in the baseline.

As mentioned above, the ^{17}O line shape methodology has the capacity to selectively detect the mobile and rigid fractions based on the differences in their effective C_q values. Due to the TRIP selectivity filter described above, for the ^{17}O data, the "free" state samples layers with the effective C_q~0, thus it selects components undergoing fast symmetrical motions. While at high temperatures all hydration layers are seen by this filter, at lower temperatures only remaining unfrozen bulk water is expected to contribute to these perfectly symmetric motions. Contributions from the loosely and tightly bound layers with high mobility but not perfectly symmetric motions are largely excluded by the C_q~0 filtering, but will be covered by the complementary large C_q measurement. The TRIP selection scheme

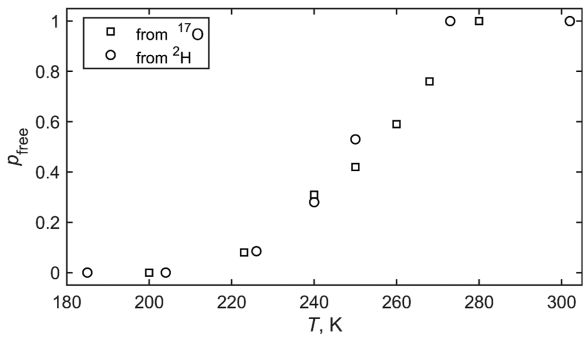

FIG. 3. Fractions of mobile (free) states of water extracted using ^{17}O and ^{2}H NMR line shape decomposition, p_{free} vs T. The errors are in the range of 0.03–0.07 for all conditions.

introduces scaling of signal intensity,[77] which needs to be taken into account in the quantitative extraction procedure of the relative fractions. Additional examples of ^{17}O line shapes as well as the details of the error analysis in the resulting values of p_{free} can be found in Fig. S4 of the supplementary material. One can also determine the approximate temperature dependence of the ^{17}O chemical shifts for the free and rigid fractions (Fig. S5 of the supplementary material).

3. Tensor parameters analysis from low-temperature line shapes

Line shapes provide direct information on the quadrupolar interactions (EFG) and chemical shift anisotropy (CSA) tensor magnitudes and their relative orientations. The EFG tensor for ^{17}O nuclei in hexagonal ice and other frozen phases of water have been previously reported.[49,61,62,65,87,88] ^{17}O low temperature spectra (Fig. 2 and Fig. S6 of the supplementary material SI2) are consistent with the quadrupolar coupling constant of C_q = 7.5 MHz and the asymmetry parameter of 0.92, which were reported for the frozen phase of water in barium chlorate monohydrate studied by Keeler *et al.*[49] We did not perform an exhaustive search of the tensor parameters but rather sought out consistency between the experiment and simulations within the ranges previously reported for bound water in salt hydrates and crystalline amino acids.[49,65]

The principal axes system of EFG has the z-axis perpendicular to the HOH plane, the y-axis along the H–H direction, and the x-axis as the HOH bisector. ^{17}O CSA interaction is expected to be minimal for the frozen water phase,[46] and while we include it in the line shape simulations of the bound state, the relaxation times data do not include this term. The ^{17}O CSA tensor parameters that we used correspond to the anisotropy of 25 ppm and the asymmetry parameter of 0.25 in Haeberlen convention,[89] with the Euler angles between the principal axes of the EFG and CSA tensors given by 0°, 0°, and 90° (Fig. S7 of the supplementary material).

An axially symmetric deuterium EFG tensor with the effective C_q = 210 kHz was used for D_2O in the hydration shells, based on the lowest temperature line shape at 169 K using the spacing between the major singularities of the powder pattern (Fig. S8 of the supplementary material). This C_q value is in the range of experimental and *ab initio* simulation values reported for water at low temperatures, as summarized in Ref. 88. Note that for pure ice it is 200–210 kHz.[88,90]

B. Relaxation data

1. Overview of the experimental relaxation data

Main relaxation measurements at both nuclei comprised longitudinal T_1 and rotating frame $T_{1\rho}$ relaxation times. ^{2}H as well as ^{17}O CT T_1 and $T_{1\rho}$ NMR relaxation decay/build-up curves were largely mono-exponential above 250–240 K (Figs. 4 and 5 and Figs. S9 and S10 of the supplementary material). ^{17}O relaxation measurements incorporated the filtering blocks for the selective detection of the water states differentiated by the effective C_q~0,

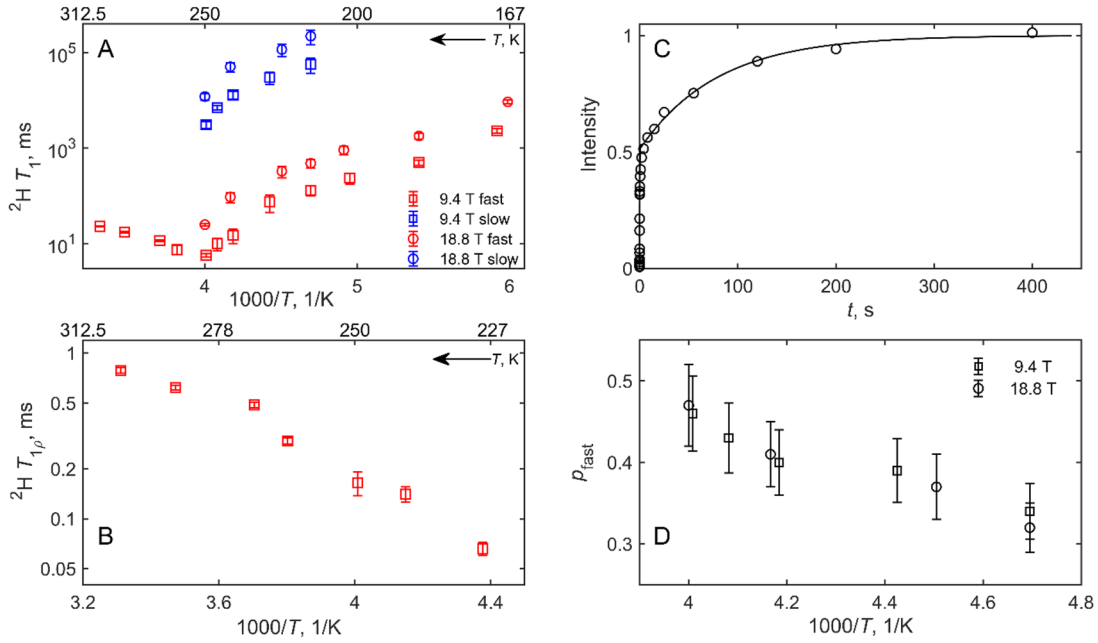

FIG. 4. 2H T_1 (a) and $T_{1\rho}$ (b) NMR relaxation times vs 1000/T of D_2O in HP36 hydrated at the 70% w/w level. The data were collected at 9.4 T only for $T_{1\rho}$ and at 9.4 and 18.8 T for T_1. The spin-locking RF field strength was 41 kHz. Magnetization build-up curves were constructed using integration of the entire powder pattern. In the 250–210 K range, the bi-exponential fits of Eq. (1) were used for longitudinal relaxation curves, resulting in two components T_1^{fast} (red) and T_1^{slow} (blue). Below 200 K the slow component is beyond the detection limit. The symbols used for the high-temperature range coincide with those used for the fast component of the low-temperature range. (c) An example of non-exponential ^{2}H T_1 magnetization build-up curve, normalized intensity vs time, obtained via the saturation recovery measurements at 240 K and 18.8 T. The solid line represents the fit to Eq. (1). (d) p_{fast} vs 1000/T extracted from the bi-exponential fits.

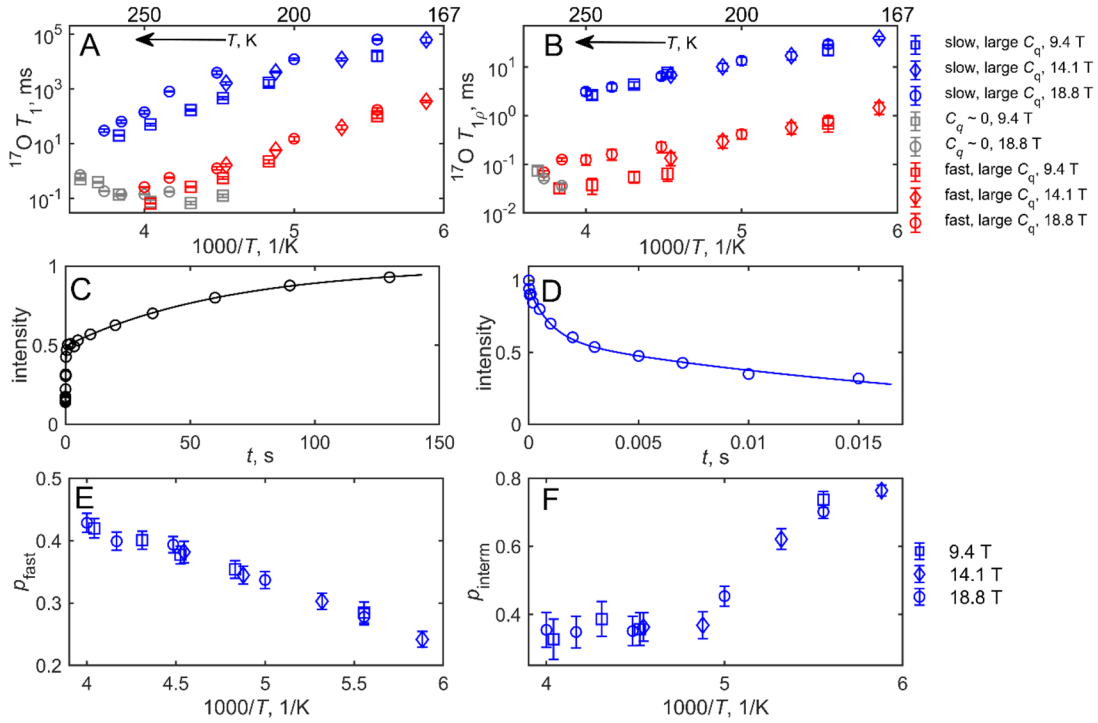

FIG. 5. ^{17}O CT T_1 (a) and $T_{1\rho}$ (b) NMR relaxation times vs 1000/T of $H_2{}^{17}O$ in HP36 at the hydration level of 70% w/w, collected at different magnetic field strengths indicated on the panels. The relaxation times of the state with the effective C_q~0, selected using the TRIP filter,[77] are color-coded in gray, while those with large C_q are color-coded separately for the fast (red) and slow (blue) relaxing components, obtained from the bi-exponential fits of Eq. (1). (c) An example of non-exponential T_1 saturation recovery build-up curve, normalized intensity vs time, at 180 K and 18.8 T, in which intensities are obtained via the integration of the entire powder pattern. The solid line shows the bi-exponential fit. (d) An example of non-exponential $T_{1\rho}$ magnetization decay curve, normalized intensity vs time, at 180 K and 18.8 T. The solid line shows the bi-exponential fit. ^{17}O $T_{1\rho}$ relaxation data were obtained using 35 kHz spin-lock RF field strength. (e) p_{fast} and (f) p_{interm} vs 1000/T, extracted from the bi-exponential fits of Eq. (1).

corresponding to states of water with fast symmetrical motions, or $C_q \gg \omega_1/2\pi$, encompassing all other water states with slow and/or non-symmetrical motions.

^{2}H $T_{1\rho}$ relaxation times were not measured below 228 K due to the significant widening of the powder pattern, precluding efficient spin-locking. This also means that only the relaxation of the mobile, motionally narrowed fraction can be seen, and the relaxation decay curves can be fitted with the mono-exponential function throughout the entire temperature range. Below 250 K, the onset of non-exponentiality was seen in the ^{2}H T_1 and ^{17}O T_1 and $T_{1\rho}$ relaxation data for the large C_q states, and the curves were fitted to the double-exponential functions (Figs. 4 and 5 and Figs. S11–S13 of the supplementary material):

$$M(t) = M_0 + (M_\infty - M_0)\left(1 - p_{fast}e^{-t/T_1^{fast}} - (1 - p_{fast})e^{-t/T_1^{slow}}\right),$$
$$M(t) = M_0\left((1 - p_{interm})e^{-t/T_{1\rho}^{fast}} + p_{interm}e^{-t/T_{1\rho}^{slow}}\right), \quad (1)$$

in which $T_{1\rho}^{fast}$, T_1^{fast} are the fast relaxing components and $T_{1\rho}^{slow}$, T_1^{slow} are the slow relaxing components; p_{fast} is the fraction of the component relaxing with the time T_1^{fast} relative to the one with the time T_1^{slow}; p_{interm} is the fraction of component relaxing with the time $T_{1\rho}^{slow}$ relative to $T_{1\rho}^{fastast}$, and M_0 for T_1 saturation recovery experiment can be somewhat different from the expected zero value due to incomplete saturation of fast-relaxing states. Thus, p_{fast} is the lower limit value. In the case of $T_{1\rho}$ double-exponential fit, no additional baseline was necessary or supported by the data.

Experimentally observed T_1^{fast} and T_1^{slow} relaxation times differ by orders of magnitude, indicating distinct mobilities originating from different hydration layers. The data shown in Figs. 4 and 5 correspond to the samples hydrated to 70% w/w water content. ^{2}H T_1^{slow} relaxation times for the slow component exceed 100 s below 200 K and cannot be measured accurately. Extremely long values of ^{2}H T_1 were also observed in pure ice at low temperature.[63] While we focus on the interpretation of the ^{2}H relaxation curves using the integrated powder patterns, at several temperatures it was possible to observe ^{2}H T_1 relaxation anisotropy, indicating the separation of the timescales for different layers from another angle (Fig. S14 of the supplementary material). The fraction of the fast-relaxing component varies from 0.47 to 0.23 [Figs. 4(d) and 5(c)], and there is a good correspondence between the ^{17}O- and ^{2}H-based fits for the range in which fractions from both data sets could be determined. Due to the employment of the TRIP filter, ^{17}O relaxation data are more

detailed in the transition region between higher and lower temperatures, from about 250 to 220 K, in which we can clearly observe separate contributions from different layers.

Below 250 K, we also probed the dependence of relaxation data on the level of hydration to elucidate in more detail the nature of non-exponential behavior. When the hydration level is changed from the 70% w/w to 40%, ^{17}O T_1^{fast} time remains approximately the same, ^{17}O T_1^{slow} has a tendency to have a somewhat lower ^{17}O T_1 value, and the fraction p_{fast} increases on average by 6% (Fig. S15 of the supplementary material). When the hydration level is reduced to 20%, the slow-relaxing component is not visible. ^{2}H T_1 relaxation data echo this result: when the level of hydration is changed to 20%, the slow-relaxing component is no longer visible. Together, these data suggest that the fast-relaxing component originates from the layer immediately adjacent to the protein surface, which remains more mobile at low temperatures. Bauer *et al.*[21] also observed the extreme separation of ^{1}H T_1 values for the protein-bound layer and bulk solvent in HET-s (218–289) fibril suspensions with high water content of 3 mg of water per 1 mg of protein. At 240 K and 9.4 T, ^{1}H T_1 values are 0.5 and 2000 s, respectively. Long ^{1}H T_1 relaxation times in bulk solvent were proposed to be governed by proton spin diffusion with ice crystal sizes on the order of 2 μm.

In contrast to the longitudinal relaxation behavior, ^{17}O $T_{1\rho}$ magnetization decay curves below about 250–240 K coincide for all hydration levels [Fig. 6(b) and Figs. S16 and S17(A) of the supplementary material]. As the "bulk" layer with long T_1 relaxation is absent in the 20% w/w hydration sample, the fact that the ^{17}O $T_{1\rho}$ relaxation curves do not depend on the hydration level suggests that the contribution from the bulk layer is very rapidly dephased by a strong dipolar network in the bulk layer due to rigid hydrogen bonds, while in mobile layers the network is disrupted due to Bjerrum defects.[91] The ^{17}O $T_{1\rho}$ magnetization decay curves also show non-exponential behavior, but its nature appears to be different from the origin of the non-exponentiality seen for longitudinal relaxation. It is possible that we observe the exchange between different hydration layers, as we will discuss in more detail in Sec. II C. ^{1}H CEST measurements under MAS by Bauer *et al.* in HET-s (218–289) fibril suspensions also suggested the existence of polarization transfer between the protein-bound water layer and the surface of the bulk frozen layer at subfreezing temperatures, occurring on the timescale of milliseconds to seconds.[21,92]

^{17}O CT T_2 relaxation times were measured in 220 to 180 K temperature range using the Hahn echo pulse sequence[76] (Fig. S18 of the supplementary material) and, unlike T_1 and $T_{1\rho}$ relaxation curves, were mono-exponential, with the values of time constant ranging from 0.4 to 1.1 ms. As we will see below, they appear to be dominated by small-angle fluctuations that are relatively similar in magnitude in all layers. Hoffmann *et al.*[63] suggested that the transverse relaxation in pure amorphous ice can be dominated by ^{17}O–^{17}O dipolar effects, based on the temperature-independence of the transverse relaxation times. The order of magnitude of T_2 times expected for the 70% ^{17}O isotope enrichment for the pure ice phase is 350 μs. Thus, if the bulk layer's contribution has this additional component, it falls within the range of T_2 times expected for small-angle fluctuations and cannot be distinguished as a separate component in our data.

At low temperatures, the 2-site proton flips are too slow to induce self-decoupling, and thus dipolar contributions from the proton network come into play. Phase-modulated proton decoupling in the presence of irradiation on ^{17}O can interfere with ^{17}O magnetization properties. Therefore, we employed cw proton decoupling at the power of 70 kHz to assess at least the heterogeneous H–O dipolar coupling effect on $T_{1\rho}$ relaxation (Fig. S19 of the supplementary material), which appears to be relatively minor. Our 9.4 T probe did not have a proton channel, and for this reason, for the field dependence of ^{17}O $T_{1\rho}$ relaxation at low temperatures, we employed a 14.1 T spectrometer with the probe capable of proton decoupling possibilities. For T_2 relaxation, SPINAL64 decoupling[82] was employed during the relaxation period, and the data were measured at 18.8 T.

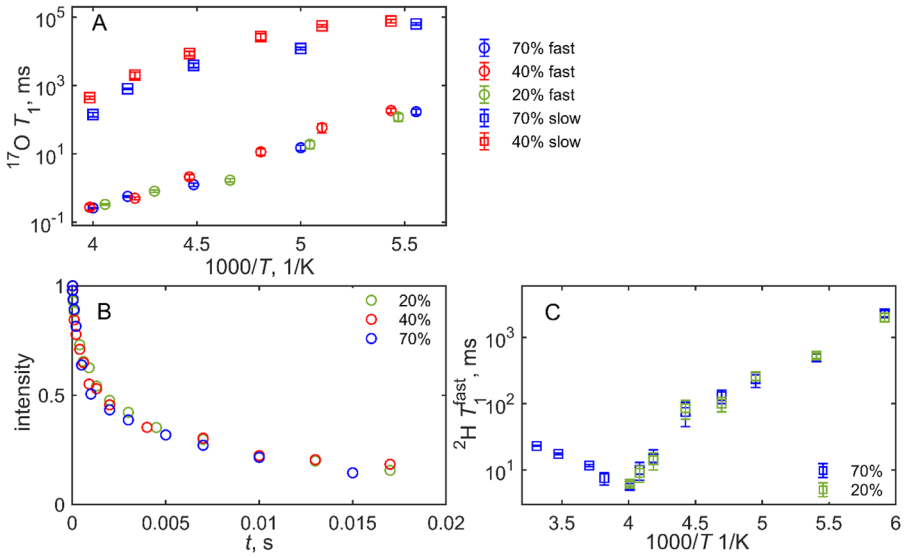

FIG. 6. Hydration-level dependence of ^{2}H and ^{17}O relaxation times in the low-temperature range. (a) ^{17}O CT longitudinal relaxation times T_1^{fast} (circles) and T_1^{slow} (squares), collected at 18.8 T. The hydration levels (w/w percentage) are shown in the legend. (b) An example of ^{17}O CT $T_{1\rho}$ magnetization decay curves collected at 18.8 T and 196–200 K temperature range for different hydration levels. (c) ^{2}H T_1^{fast} times collected at 9.4 T. The slow component is not visible for the 20% w/w hydration level for both ^{2}H and ^{17}O T_1 data.

2. Overview of the motional modes

In discussing motional modes, we will start with the largest amplitude modes and progressively introduce smaller-amplitude and less symmetric modes as dictated by the data. The development of the motional models is guided by the minimal number of modes constructed in this hierarchical fashion needed to explain the data.

The largest in amplitude, and the most symmetric type of motion, is diffusion of water molecules (Fig. 7). While the assumption of isotropic motions in the solid state is obviously an approximation, it provides the correct order of magnitude for the diffusion coefficient. Next in the amplitude scale of motional modes are changes in the water molecule orientations that approximately preserve its coordination within the local environment of the water molecule. These types of motions have been invoked in a variety of systems. There are 12 such orientations overall.[21,93,94] Two of them, different only by the exchange of the positions of hydrogen nuclei, will be preferred due to minimal perturbations in the hydrogen bonds, and we refer to them as 2-site proton or deuteron flips. The interchange between the two deuteron nuclei is expected to be a much faster mode than any other reorientation within the overall 12 positions.

The ^{17}O quadrupolar tensor is not changed due to the proton flips. Therefore, another subset of the tetrahedral reorientations, which involves changes in the location of at least one of the hydrogen nuclei, is needed to explain ^{17}O relaxation. This subset spans six sites, symmetrical with respect to the proton positions. The populations of these six sites can be skewed due to an anisotropic environment. Usually, a single orientation out of six possible ones is preferred because it is the most favorable for the creation of the hydrogen bonding network. As we will see below, experimental data supports the conclusion of the presence of one major state. We assume, for simplicity, that in addition to this major orientation only one other minor state remains significantly populated. While in relatively unrestricted water layers [such as bulk and loosely bound layers shown in Fig. 1(b)] the two sites can involve large changes in the positions of both hydrogens, the situation is more restricted for the water layer immediately adjacent to the protein surface [Fig. 1(c)]. This layer can participate in transient hydrogen bonds with polar side-chain and backbone sites of the protein, and thus the tetrahedral jump would involve pivoting of the water molecule around the hydrogen bond axis. Using two orientations out of possible 6 (or 3 when one proton remains bound to the protein surface) is, of course, a simplification. However, the available data do not allow us to distinguish between the number of minor orientations and would be fit equally well with different choices of the number of states. We will comment more on this issue below when discussing fits to the reorientation modes.

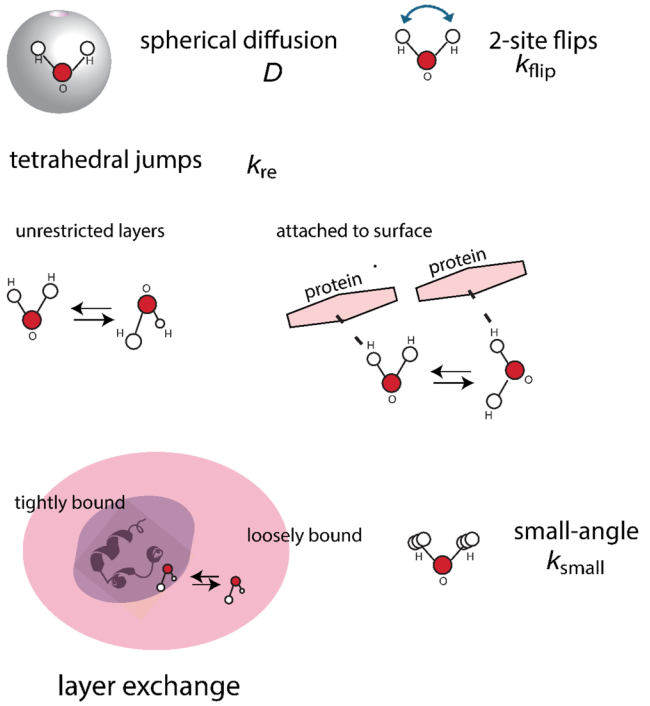

FIG. 7. Graphical representation of the motional modes of water molecules in the hydrated shells of proteins and associated definitions of the rate constants. The modes shown are in the approximate order of diminishing amplitudes and symmetries: diffusion, approximated as isotropic; 2-site proton flips; 2-site tetrahedral reorientations in two variations: either the change in the position of both hydrogens or pivoting along the transient hydrogen bond axis due to interactions with the protein surface, small-angle fluctuations, and exchange between layers due to translational diffusion.

TABLE I. Summary of motional modes as seen by each experiment for different hydration layers.

Motion		Water layers		
		Bulk	Loosely bound	Tightly bound
Rotational diffusion		302–220 K, ^{2}H T_1, $T_{1\rho}$	302–220 K, ^{2}H T_1, $T_{1\rho}$	
2-site proton flips		All layers, 302–220 K, ^{2}H T_1, $T_{1\rho}$ and 220–170 K, ^{2}H T_1		
Tetrahedral reorientations	Unrestricted	280–220 K, ^{17}O T_1, $T_{1\rho}$	280–220 K, ^{17}O T_1, $T_{1\rho}$	
	Attached to surface			250–170 K, ^{17}O T_1, $T_{1\rho}$
Small-angle		268–170 K, ^{17}O T_1		
Exchange between layers			250–170 K, ^{17}O T_1, $T_{1\rho}$	250–170 K, ^{17}O T_1, $T_{1\rho}$

Finally, the smallest amplitude mode consists of local bending/twisting motions of water molecules. An additional dynamic mode can involve exchange between adjacent water layers due to translational diffusion.

The sensitivity of the NMR relaxation rates to the motional modes is shown in Fig. S20 of the supplementary material, displaying simulated relaxation times as a function of rate constants. The trends in T_1 and $T_{1\rho}$ relaxation times emphasize the necessity of employing wide temperature ranges and multiple relaxation experiments for establishing motional modes and their regimes of dominance. Table I summarizes the types of motional modes present in each layer as revealed by different NMR relaxation experiments. The line shape data are used to obtain relative fractions of different layers.

3. Fits to the motional models, high temperature range for the free fraction

In the high to intermediate temperature range spanning 302–220 K, multiple modes of motion can be present for all hydration layers. We will first discuss this temperature regime and focus on the subspace of ^{17}O $C_q \sim 0$ states representing the "free" fraction in Fig. 3. ^{2}H T_1 data were based on the integrated intensities over the entire spectral range, and thus, the resulting parameters originate from all water layers. However, for the ^{2}H $T_{1\rho}$ measurements, the spin-locking field of 41 kHz effectively filters contributions from the more rigid layers, which are not locked under these conditions.

NMR relaxation times have differential sensitivity to the motional modes, governed by the interplay between the timescales of motion, quadrupolar coupling constant, the Larmor frequency, and the RF field strength in the case of rotating-frame relaxation (Fig. S20 of the supplementary material). Thus, ^{2}H $T_{1\rho}$ is expected to be most sensitive to the diffusion mode, while ^{2}H T_1 is most sensitive to the faster motions of the 2-site deuteron flips mode. ^{2}H relaxation data were thus fitted with the joint modes of diffusion and 2-site flips. The diffusion mode had minimal effect below about 240 K, and was excluded entirely below 220 K. The resulting rate constant k_{flip} and diffusion coefficient D, as a function of inverse temperature, are shown in Figs. 8(a) and 8(b). The temperature dependence of k_{flip} can be fitted in Arrhenius fashion, with an activation energy of 24 ± 2 kJ/mol and the Arrhenius pre-factor lnk_0 of 33 ± 1 in the 302–250 K temperature range.

Relaxation at the ^{17}O nuclei is insensitive to the 2-site proton flips, but is very sensitive to the tetrahedral reorientation motions, as well as diffusion at high temperatures when it is fast

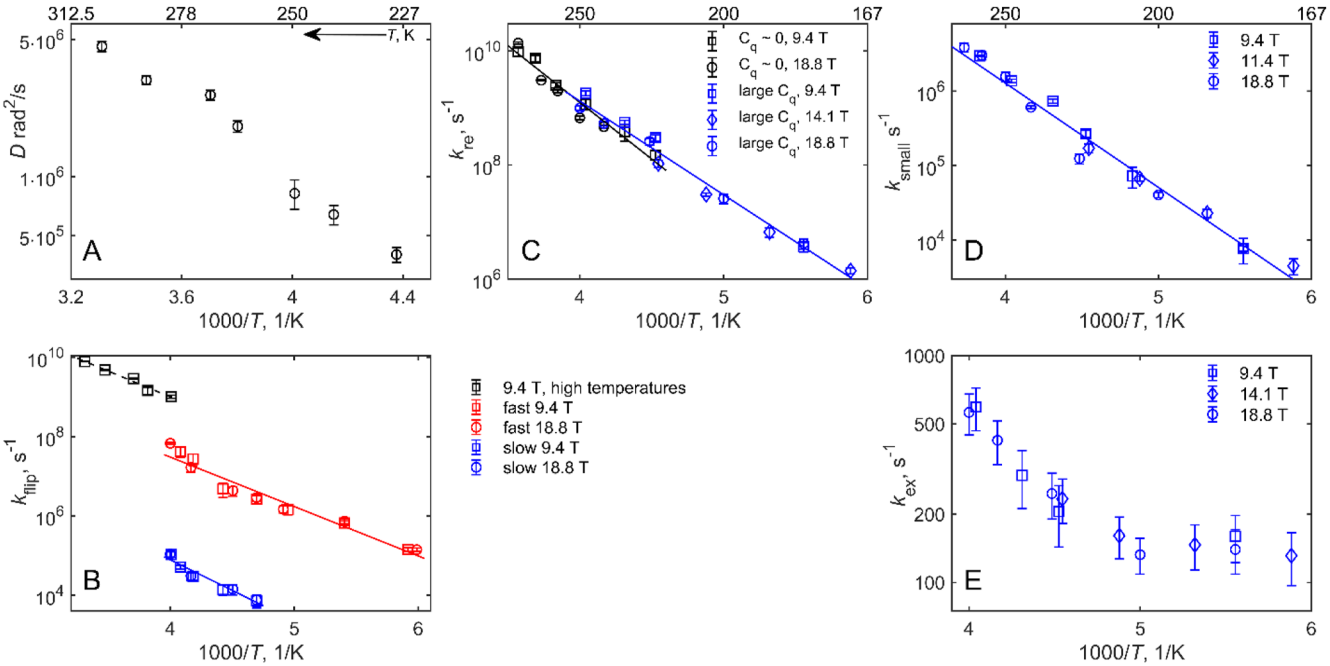

FIG. 8. (a) Rotational diffusion coefficient, D vs 1000/T, for mobile (bulk and loosely bound) hydration layers obtained from ^{2}H NMR relaxation times at 9.4 T in the 302–228 K temperature range. (b) 2-site deuteron flip rate constants k_{flip} vs 1000/T, obtained from ^{2}H NMR relaxation data. The high temperature range of 302–250 K (black squares) incorporates contributions from all layers of water; the low temperature range shows separate fits obtained either from ^{2}H T_1^{fast} times (red symbols) or ^{2}H T_1^{slow} times (blue symbols). (c) The rate constants for the 2-site tetrahedral reorientations obtained on the basis of ^{17}O NMR relaxation data: k_{re} vs 1000/T for the free state/small C_q subspace (black symbols) and the tightly bound state immediately adjacent to the protein surface, large C_q subspace (blue symbols). The ratio of the 2-site tetrahedral populations is taken as 9:1. (d) The rate constant for small-angle fluctuations, k_{small} vs 1000/T, obtained on the basis of ^{17}O NMR T_1^{slow} relaxation data. The amplitude of small-angle fluctuations is taken as 15°. (e) The rate constant for the exchange between protein-bound and adjacent layers, k_{ex} vs 1000/T, obtained from the ^{17}O $T_{1\rho}$ data. All data are shown for the HP36 protein hydrated at 70% w/w level with either D_2O or $H_2{}^{17}O$. The corresponding magnetic field values at which the data were collected are shown directly in the legends.

enough to approach the Larmor frequency. The diffusion coefficient approaches this limit only at temperatures above the bulk freezing point of water. Unequal populations of the two-site tetrahedral jumps mode (denoted by "unrestricted layers" caption in Fig. 8) are required to fit ^{17}O T_1 relaxation times; otherwise, the experimental value of the T_1 minimum could not be reached (Fig. S21 of the supplementary material). The best-fit value of the ratio of the two populations was 9:1, underscoring a restricted environment. The rate constant, k_{re}, follows a relatively well-pronounced Arrhenius behavior, with an activation energy of 38 ± 3 kJ/mol [Fig. 8(c)] and the Arrhenius pre-factor lnk_0 of 40 ± 1.

If instead of a single minor orientation, two equally populated minor orientations are considered, then the data can be fit with the weight of the major state of 0.93 and values of k_{re} lowered by a factor of 0.8. For a model with five equally populated minor orientations, the weight of the major state must be raised to 0.96 and k_{re} decreased by a factor of 0.4. In all cases, k_{re} is defined as the sum of the forward and backward exchange rates between the major and any of the minor states.

4. Fits to the motional models, low-temperature range below 250 K for protein-bound and frozen layers

As shown in Section II B.1 (Figs. 4–6), ^{2}H T_1 and ^{17}O T_1 relaxation data for the large C_q subspace are split into two fractions, with the fast-relaxing component corresponding to the layer tightly bound to the protein surface. We hypothesize that this layer retains a certain degree of large-angle fluctuations, mediated by interactions with the protein surface, such as transient hydrogen bonding to the exchangeable sites on the protein surface [see Fig. 1(c) as an example]. One possible scenario is the retention of 2-site tetrahedral jumps while one of the hydrogen atoms is anchored to the protein surface. The assumption of this specific model is given as an example, with minimal changes to water geometry. This mode is consistent with models for water found in the literature, based on Bjerrum-type defects.[91] Additional constraints on the populations of the 2-site tetrahedral states are given by the correlation of experimental values of ^{17}O $T_{1\rho}^{fast}$ and ^{17}O T_1^{fast} times (Fig. S22 of the supplementary material). Based on the analysis, the weight of the minor conformer was taken as 10% for all temperatures, which is identical to the population used for fits of the free fraction spanning the small C_q subspace. Invoking temperature-dependent populations in this case would likely lead to overfitting the data. The fitted values of k_{re} based on ^{17}O relaxation times are shown in Fig. 8(c) in blue symbols. The trend in the temperature dependence of k_{re} can be fitted with the Arrhenius model, yielding an activation energy of 32 ± 1 kJ/mol and an Arrhenius pre-factor lnk_0 of 36 ± 1. It is interesting to note that the rotameric jumps in the protein-bound layer follow the same trend in k_{re} and its temperature dependence as the mobile layers from the small C_q subspace.

As hypothesized in Sec. II A, because ^{17}O $T_{1\rho}$ curves remain the same for all levels of hydration [Fig. 6(b) and Fig. S16 of the supplementary material], the ^{17}O T_1^{slow} component may originate from exchange between the layer immediately adjacent to the protein surface and a few layers further away. The origin of exchange could be translational diffusion of water molecules and dipolar-mediated polarization transfer. Additional arguments in support of the exchange model are presented in SI3. The bi-exponential fits of the ^{17}O $T_{1\rho}$ magnetization decay curves yield the approximate relative fraction of the exchanging layer relative to the layer immediately adjacent to the protein surface, p_{inter}, in the 0.35–0.75 range [Fig. 5(f) and Fig. S17 of the supplementary material]. Under this assumption, the values of the exchange rate constant k_{ex} can be extracted [Fig. 8(e) and Fig. S17 of the supplementary material] and they range between 600 and 160 s^{-1}. Values of k_{ex} can be roughly estimated in the $T_{1\rho}^{fast} \ll T_{1\rho}^{slow}$ limit as $k_{ex} \sim T_{1\rho}^{slow}/(1 - p_{inter})$. More precise calculations require solving McConnell equations (SI1).[95]

The bi-exponential ^{2}H T_1 decay curves for HP36 hydrated to 70% w/w indicate that the 2-site deuteron flips differ by orders of magnitude between the layer immediately adjacent to the protein surface and the layers further away. Indeed, the fit to the 2-site flip model for the fast- and slow- relaxing components quantitatively demonstrates this conclusion [Fig. 8(b)]. It is also seen that the value of k_{flip} drops by a factor of 30 upon the onset of non-exponentiality at 250 K. As mentioned above, the slow-relaxing component disappears in the sample with 20% w/w hydration, implying that the layers in immediate proximity to the protein surface retain multiple modes of increased mobility, including large-angle tetrahedral reorientations and the 2-site flips. The k_{flip} rate constants for the fast components do not depend on the hydration level, as evident from the correspondence of ^{2}H T_1^{fast} times for the two samples with hydration levels of 70% and 20% w/w [Fig. 6(c)]. Interestingly, the activation energies for the 2-site flips are rather similar for the fast and slow components, in the 24–30 kJ/mol range and are also comparable to the activation energy for the flipping motion in the high-temperature range. The similarities in activation energies imply that they are likely stemming from the H-bond distortion of the single water molecule experiencing the flipping motion. The differences in flipping rate constants thus appear to stem from variations in the values of k_0, which is governed by the effect of the overall environment and not just the immediate hydrogen bond. Contributions from entropic factors into the "transition state" of the H-bond breaking and concurrent flipping motion also come into play. The values of lnk_0 are 33 ± 1, 29 ± 1, and 26 ± 1 for the high temperature range, fast-relaxing protein-bound layer at low temperature, and slow-relaxing layers at low temperatures, respectively. In the slow-relaxing layers away from the protein surface, the 2-site flips are significantly slowed, with the lowest measured value of 7.5 × 10^3 s^{-1} at 213 K and the projected value of 60 s^{-1} at 170 K, based on the Arrhenius dependence. As stated above, below about 200 K the ^{2}H T_1^{slow} component increases beyond the measurement limit.

The slow-relaxing component ^{17}O T_1^{slow} spans the range from 141 ms to 68 s at 18.8 T when the temperature is in the 250–170 K range and is associated with the water layers away from the protein surface (loosely bound and bulk). There are minor variations in the magnitude of this component between the 70% and 40% w/w hydration levels (Fig. 6), and the slow component is nonexistent at the 20% hydration level. This slow relaxation indicates that large-amplitude motions are frozen and that the relaxation is dominated by small-amplitude fluctuations. ^{17}O T_1^{slow} data alone cannot define the amplitude of fluctuations, but the T_2/T_1 ratio can provide these constraints when the T_1 data is in the slow regime with respect to the Larmor frequency. Thus, we collected T_2 data at three temperatures—220, 200, and 180 K at 18.8 T—for the 70%

w/w hydration level sample (Fig. S18 of the supplementary material). In contrast to both T_1 and $T_{1\rho}$ relaxation, T_2 data are mono-exponential, suggesting that there is little distinction in timescale among all water layers. T_2 times were rather short, between 0.4 and 1.1 ms, indicating effective relaxation. Simulations according to small-angle fluctuations [Fig. S23(A) of the supplementary material] reveal that when T_1 is in the slow motional regime and the values are long, T_2 relaxation remains effective. This suggests that small-angle fluctuations are the dominant mechanism of T_2 relaxation in all water layers. The T_2 vs T_1 correlation plot constrains the angle within the 7°–20° range for these temperatures [Fig. S23(B) of the supplementary material]. However, we chose to use a uniform angle of 15° for all temperatures not to overfit the data. The values of T_1^{slow} at all three fields were thus fitted to this mode to yield the rate constant [Fig. 6(a) and Fig. S17(C) of the supplementary material]. The temperature dependence is approximately Arrhenius, with an activation energy value of 27 ± 1 kJ/mol.

Small-angle fluctuations are also expected to be present in the D_2O-hydrated samples down to at least 170 K, where the measurements are conducted. We use an effective ^{2}H C_q value of 210 kHz across the entire temperature range, implying that these fluctuations remain constant in amplitude and are in the fast motional regime with respect to the quadrupolar coupling constant. While this is obviously an approximation, within the precision of the data and the low-temperature spectrum presented in Fig. S8 of the supplementary material, including the temperature dependence of the effective C_q value would be an overfitting in our case. A side effect of this treatment is that the k_{flip} rate constant implicitly carries additional temperature dependence.

C. Discussion of the interconnection between hydration water and protein dynamics

We have seen that below 250 K, the separation between the behaviors of different hydration layers becomes more pronounced, and the dynamical features of these layers can be specified more precisely when hydration-level dependence is analyzed in the 20%–70% w/w range. This highlights the microscopic origins of the water changes potentially governing the coupling of water and protein modes. Of particular note is the retention of the large-angle motions in the layer immediately adjacent (tightly bound) to the surface, and the way its mobility is indirectly transferred to neighboring layers via translational diffusion, while the "bulk" layers further away from the surface experience a distinct rigidification. We have previously observed the effect of hydration on the dynamics of side chains in the core of HP36 using deuterium NMR, noting that dehydration significantly suppresses large-amplitude motions. In particular, at 40% hydration level, ring-flipping motions dominate the dynamics down to about 240 K and decrease significantly at 200 K for the F51 and F58 side chains, while in the dry protein, the ring flips are significantly suppressed below 280 K, and the activation energy for the ring-flipping motion increases by a factor of 1.5.[74] Hydration water also had a profound effect on rotameric interconversion of several key methyl-bearing side chains of HP36 (V50, L61, and L75), effectively suppressing these motions in the dry state compared to the 40% hydration level.[75] At 40% hydration level, large-amplitude rotameric jumps were effective down to at least 250 K, as judged from deuterium line shapes. Both the hydrophobic core ring-flipping motions and the large-scale rotameric jumps of the side chains are known to involve concerted fluctuations of the entire core region,[96,97] thus underpinning the importance of hydration shells for the enhancement of the overall hydrophobic core flexibility.

IV. CONCLUSION

We demonstrated the power of combined analysis of ^{2}H and ^{17}O solid-state NMR line shape and relaxation times to elucidate water dynamics in protein systems in the semi-solid states of rehydrated powders. Due to the differential sensitivities of the experiments to timescales of motion and the ability to manipulate pulse sequences to probe different hydration layers of water, we can obtain precise motional mechanisms and determine rate constants over a broad temperature range. As a result, we have obtained a detailed picture of the motional modes (Fig. 7), their predominant regimes, and temperature dependence. Distinct bi-exponential features of ^{2}H and ^{17}O relaxation at low temperatures point to sharp differences in the dynamics of the layer immediately adjacent to the protein surface and those further away. We hypothesize that this layer interacts with the surface by forming hydrogen bonds with polar protein side chains and possibly the backbone, thus creating unique packing for the inner water layer, which is capable of retaining high mobility down to low temperatures. Hydration dependence of the dynamics corroborated the distinction between the layers and established the influence of the protein surface on their dynamics. The mobility of the tightly bound layer is retained for the modes of tetrahedral jumps and 2-site proton flips. In contrast, the rate constants for the bulk layers decrease by orders of magnitude for these modes. The onset of non-exponentiality occurs around 250 K and is close to the temperature at which proteins are known to undergo the dynamical transition—above which large-amplitude concerted motions are activated in the protein itself. Around this temperature, large-amplitude motions involving concerted fluctuations of core side chains are active in the hydrated state of HP36 but are suppressed in the dry state.

SUPPLEMENTARY MATERIAL

Supplementary material for structures, experimental results, and simulations are provided in Figs. S1–S23, as well as additional description of the motional models and simulations in SI1–3.

DEDICATION

L.V. dedicates this paper to her father Boris E. Vugmeister, a well-known solid-state physicist, who passed away while the manuscript was written: *to my father, who taught me what science means.*

ACKNOWLEDGMENTS

Several experiments were performed at the National High Magnetic Field Laboratory, which is supported by NSF Cooperative Agreement No. NSF/DMR-2128556, the State of Florida, and the U.S. Department of Energy. A part of this work was supported by the National Institutes of Health Grant No. R15-GM111681 to L.V.

We thank Dr. Eric Keeler for providing the SIMPSON simulations script.

AUTHOR DECLARATIONS

Conflict of Interest

The authors have no conflicts to disclose.

Author Contributions

Liliya Vugmeyster: Conceptualization (equal); Formal analysis (equal); Funding acquisition (lead); Investigation (lead); Methodology (equal); Writing – original draft (lead); Writing – review & editing (lead). **Bailey Frazier**: Investigation (supporting); Writing – review & editing (supporting). **Riqiang Fu**: Investigation (supporting); Methodology (supporting); Resources (equal); Writing – review & editing (supporting). **Dmitry Ostrovsky**: Conceptualization (equal); Formal analysis (equal); Funding acquisition (supporting); Investigation (equal); Methodology (equal); Software (lead); Writing – original draft (supporting); Writing – review & editing (equal).

DATA AVAILABILITY

The data that support the findings of this study are available from the corresponding author upon reasonable request.

REFERENCES

[1]M. J. Ryan, L. Gao, F. I. Valiyaveetil, A. A. Kananenka, and M. T. Zanni, "Water inside the selectivity filter of a K+ ion channel: Structural heterogeneity, picosecond dynamics, and hydrogen bonding," J. Am. Chem. Soc. **146**, 1543–1553 (2024).
[2]M. D. Gelenter, V. S. Mandala, M. J. M. Niesen, D. A. Sharon, A. J. Dregni, A. P. Willard, and M. Hong, "Water orientation and dynamics in the closed and open influenza B virus M2 proton channels," Commun. Biol. **4**, 338 (2021).
[3]G. I. Makhatadze and P. L. Privalov, "Contribution of hydration to protein folding thermodynamics," J. Mol. Biol. **232**, 639–659 (1993).
[4]V. Kurkal, R. M. Daniel, J. L. Finney, M. Tehei, R. V. Dunn, and J. C. Smith, "Enzyme activity and flexibility at very low hydration," Biophys. J. **89**, 1282–1287 (2005).
[5]D. Thirumalai, G. Reddy, and J. E. Straub, "Role of water in protein aggregation and amyloid polymorphism," Acc. Chem. Res. **45**, 83–92 (2012).
[6]A. C. Fogarty, E. Duboué-Dijon, F. Sterpone, J. T. Hynes, and D. Laage, "Biomolecular hydration dynamics: A jump model perspective," Chem. Soc. Rev. **42**, 5672–5683 (2013).
[7]B. Halle, "Protein hydration dynamics in solution: A critical survey," Philos. Trans. R. Soc. London, Ser. B **359**, 1207–1224 (2004).
[8]K. Sasaki, I. Popov, and Y. Feldman, "Water in the hydrated protein powders: Dynamic and structure," J. Chem. Phys. **150**, 204504 (2019).
[9]M. Tarek and D. J. Tobias, "The dynamics of protein hydration water: A quantitative comparison of molecular dynamics simulations and neutron-scattering experiments," Biophys. J. **79**, 3244–3257 (2000).
[10]T. Wang, H. Jo, W. F. DeGrado, and M. Hong, "Water distribution, dynamics, and interactions with Alzheimer's β-amyloid fibrils investigated by solid-state NMR," J. Am. Chem. Soc. **139**, 6242 (2017).
[11]M. C. Bellissent-Funel, A. Hassanali, M. Havenith, R. Henchman, P. Pohl, F. Sterpone, D. van der Spoel, Y. Xu, and A. E. Garcia, "Water determines the structure and dynamics of proteins," Chem. Rev. **116**, 7673–7697 (2016).
[12]A. C. Fogarty and D. Laage, "Water dynamics in protein hydration shells: The molecular origins of the dynamical perturbation," J. Phys. Chem. B **118**, 7715–7729 (2014).
[13]C. Mattea, J. Qvist, and B. Halle, "Dynamics at the protein-water interface from ^{17}O spin relaxation in deeply supercooled solutions," Biophys. J. **95**, 2951–2963 (2008).
[14]S. R. Natesh, A. R. Hummels, J. R. Sachleben, T. R. Sosnick, K. F. Freed, J. F. Douglas, S. C. Meredith, and E. J. Haddadian, "Molecular dynamics study of water channels in natural and synthetic amyloid-β fibrils," J. Chem. Phys. **154**, 235102 (2021).
[15]M. Maurer and C. Oostenbrink, "Water in protein hydration and ligand recognition," J. Mol. Recognit. **32**, e2810 (2019).
[16]D. Laage, T. Elsaesser, and J. T. Hynes, "Water dynamics in the hydration shells of biomolecules," Chem. Rev. **117**, 10694–10725 (2017).
[17]J. M. Franck and S. Han, "Chapter five - Overhauser dynamic nuclear polarization for the study of hydration dynamics, explained," in *Methods in Enzymology*, edited by A. J. Wand (Academic Press, 2019), pp. 131–175.
[18]D. Kruk, A. Kasparek, E. Masiewicz, K. Kolodziejski, R. Cybulski, and B. Nowak, "Water dynamics in highly concentrated protein systems—Insight from nuclear magnetic resonance relaxometry," Int. J. Mol. Sci. **24**, 4093 (2023).
[19]N. Miura, Y. Hayashi, N. Shinyashiki, and S. Mashimo, "Observation of unfreezable water in aqueous solution of globule protein by microwave dielectric measurement," Biopolymers **36**, 9–16 (1995).
[20]T. Miyatou, T. Araya, R. Ohashi, T. Ida, and M. Mizuno, "Hydration water dynamics in bovine serum albumin at low temperatures as studied by deuterium solid-state NMR," J. Mol. Struct. **1121**, 80–85 (2016).
[21]T. Bauer, J. Gath, A. Hunkeler, M. Ernst, A. Böckmann, and B. H. Meier, "Hexagonal ice in pure water and biological NMR samples," J. Biomol. NMR **67**, 15–22 (2017).
[22]F. Persson, P. Söderhjelm, and B. Halle, "How proteins modify water dynamics," J. Chem. Phys. **148**, 215103 (2018).
[23]W. Doster, "The dynamical transition of proteins, concepts and misconceptions," Eur. Biophys. J. **37**, 591–602 (2008).
[24]S. Khodadadi and A. P. Sokolov, "Protein dynamics: From rattling in a cage to structural relaxation," Soft Matter **11**, 4984–4998 (2015).
[25]D. Ringe and G. A. Petsko, "The 'glass transition' in protein dynamics: What it is, why it occurs, and how to exploit it," Biophys. Chem. **105**, 667–680 (2003).
[26]R. B. Best, J. Clarke, and M. Karplus, "The origin of protein sidechain order parameter distributions," J. Am. Chem. Soc. **126**, 7734–7735 (2004).
[27]Y. Miyazaki, T. Matsuo, and H. Suga, "Low-temperature heat capacity and glassy behavior of lysozyme crystal," J. Phys. Chem. B **104**, 8044–8052 (2000).
[28]M. Karplus, D. Vitkup, D. Ringe, and G. A. Petsko, "Solvent mobility and the protein 'glass' transition," Nat. Struct. Biol. **7**, 34–38 (2000).
[29]J. R. Lewandowski, M. E. Halse, M. Blackledge, and L. Emsley, "Direct observation of hierarchical protein dynamics," Science **348**, 578–581 (2015).
[30]S. Khodadadi, S. Pawlus, J. H. Roh, V. Garcia Sakai, E. Mamontov, and A. P. Sokolov, "The origin of the dynamic transition in proteins," J. Chem. Phys. **128**, 5 (2008).
[31]W. Doster, "The two-step scenario of the protein dynamical transition," J. Non-Cryst. Solids **357**, 622–628 (2011).
[32]S. Khodadadi, A. Malkovskiy, A. Kisliuk, and A. P. Sokolov, "A broad glass transition in hydrated proteins," Biochim. Biophys. Acta, Proteins Proteomics **1804**, 15–19 (2010).
[33]Y. Miao, Z. Yi, D. C. Glass, L. Hong, M. Tyagi, J. Baudry, N. Jain, and J. C. Smith, "Temperature-dependent dynamical transitions of different classes of amino acid residue in a globular protein," J. Am. Chem. Soc. **134**, 19576–19579 (2012).
[34]J. H. Roh, V. N. Novikov, R. B. Gregory, J. E. Curtis, Z. Chowdhuri, and A. P. Sokolov, "Onsets of anharmonicity in protein dynamics," Phys. Rev. Lett. **95**, 038101 (2005).
[35]J. C. McKnight, D. S. Doering, P. T. Matsudaira, and P. S. Kim, "A thermostable 35-residue subdomain within villin headpiece," J. Mol. Biol. **260**, 126–134 (1996).
[36]A. Bretscher and K. Weber, "Villin is a major protein of the microvillus cytoskeleton which binds both G and F actin in a calcium-dependent manner," Cell **20**, 839–847 (1980).

[37]T. K. Chiu, J. Kubelka, R. Herbst-Irmer, W. A. Eaton, J. Hofrichter, and D. R. Davies, "High-resolution x-ray crystal structures of the villin headpiece subdomain, an ultrafast folding protein," Proc. Natl. Acad. Sci. U. S. A. **102**, 7517–7522 (2005).
[38]C. J. McKnight, P. T. Matsudaira, and P. S. Kim, "NMR structure of the 35-residue villin headpiece subdomain," Nat. Struct. Biol. **4**, 180–184 (1997).
[39]J. K. Williams and M. Hong, "Probing membrane protein structure using water polarization transfer solid-state NMR," J. Magn. Reson. **247**, 118–127 (2014).
[40]E. G. Keeler, V. K. Michaelis, C. B. Wilson, I. Hung, X. Wang, Z. Gan, and R. G. Griffin, "High-resolution ^{17}O NMR spectroscopy of structural water," J. Phys. Chem. B **123**, 3061–3067 (2019).
[41]T. Sun, F. H. Lin, R. L. Campbell, J. S. Allingham, and P. L. Davies, "An antifreeze protein folds with an interior network of more than 400 semi-clathrate waters," Science **343**, 795–798 (2014).
[42]B. Yu, M. Blaber, A. M. Gronenborn, G. M. Clore, and D. L. D. Caspar, "Disordered water within a hydrophobic protein cavity visualized by x-ray crystallography," Proc. Natl. Acad. Sci. U. S. A. **96**, 103–108 (1999).
[43]M. Liao, E. Cao, D. Julius, and Y. Cheng, "Structure of the TRPV1 ion channel determined by electron cryo-microscopy," Nature **504**, 107–112 (2013).
[44]B. D. Armstrong, J. Choi, C. López, D. A. Wesener, W. Hubbell, S. Cavagnero, and S. Han, "Site-specific hydration dynamics in the nonpolar core of a molten globule by dynamic nuclear polarization of water," J. Am. Chem. Soc. **133**, 5987–5995 (2011).
[45]P. N. Gallo, J. C. Iovine, and N. V. Nucci, "Toward comprehensive measurement of protein hydration dynamics: Facilitation of NMR-based methods by reverse micelle encapsulation," Methods **148**, 146–153 (2018).
[46]G. Wu, "^{17}O NMR studies of organic and biological molecules in aqueous solution and in the solid state," Prog. Nucl. Magn. Reson. Spectrosc. **114-115**, 135–191 (2019).
[47]L. Piculell, "Water spin relaxation in colloidal systems. Part 1.—^{17}O and ^{2}H relaxation in dispersions of colloidal silica," J. Chem. Soc., Faraday Trans. 1 **82**, 387–399 (1986).
[48]D. Goldfarb, H. X. Li, and M. E. Davis, "Dynamics of water molecules in VPI-5 and AlPO4-5 studied by deuterium NMR spectroscopy," J. Am. Chem. Soc. **114**, 3690–3697 (1992).
[49]E. G. Keeler, V. K. Michaelis, and R. G. Griffin, "^{17}O NMR investigation of water structure and dynamics," J. Phys. Chem. B **120**, 7851–7858 (2016).
[50]L. Vugmeyster, T. Do, D. Ostrovsky, R. Fu, and B. Hagedorn, "Characterization of water dynamics in frozen soils by solid-state deuteron NMR," Solid State Nucl. Magn. Reson. **45-46**, 11–15 (2012).
[51]T. Sparrman, M. Öquist, L. Klemedtsson, J. Schleucher, and M. Nilsson, "Quantifying unfrozen water in frozen soil by high-field ^{2}H NMR," Environ. Sci. Technol. **38**, 5420–5425 (2004).
[52]S. Nour, C. M. Widdifield, L. Kobera, K. M. N. Burgess, D. Errulat, V. V. Terskikh, and D. L. Bryce, "Oxygen-17 NMR spectroscopy of water molecules in solid hydrates," Can. J. Chem. **94**, 189–197 (2016).
[53]C. Tobar, R. Cordova, T. Solomon, K. Palombo, G. Olivares, J. Helston, W. Luo, D. Cizmeciyan, and A. Benesi, "Water dynamics in deuterated gypsum, $CaSO_4{\cdot}2D_2O$, investigated by solid state deuterium NMR," J. Magn. Reson. **310**, 106640 (2020).
[54]M. El Hariri El Nokab, A. Lasorsa, K. O. Sebakhy, F. Picchioni, and P. C. A. van der Wel, "Solid-state NMR spectroscopy insights for resolving different water pools in alginate hydrogels," Food Hydrocolloids **127**, 107500 (2022).
[55]K. J. Ooms, A. J. Vega, T. Polenova, M. Cannella, and M. Marcolongo, "Double and zero quantum filtered ^{2}H NMR analysis of D_2O in intervertebral disc tissue," J. Magn. Reson. **258**, 6–11 (2015).
[56]R. Nath, A. Nowaczyk, B. Geil, and R. Böhmer, "^{2}H NMR studies of supercooled and glassy aspirin," J. Non-Cryst. Solids **353**, 3788–3795 (2007).
[57]N. Weerasinghe, S. M. D. C. Perera, T. R. Molugu, and M. F. Brown, "Functional water dynamics in rhodopsin using solid-state deuterium NMR spectroscopy," FASEB J. **33**, 655.659 (2019).
[58]B. Borah and R. G. Bryant, "Deuterium NMR of water in immobilized protein systems," Biophys. J. **38**, 47–52 (1982).
[59]K. Modig, J. Qvist, C. B. Marshall, P. L. Davies, and B. Halle, "High water mobility on the ice-binding surface of a hyperactive antifreeze protein," Phys. Chem. Chem. Phys. **12**, 10189–10197 (2010).
[60]S. A. Lusceac, M. R. Vogel, and C. R. Herbers, "^{2}H and ^{13}C NMR studies on the temperature-dependent water and protein dynamics in hydrated elastin, myoglobin and collagen," Biochim. Biophys. Acta, Proteins Proteomics **1804**, 41–48 (2010).
[61]K. Yamada, K. Deguchi, T. Shimizu, and J. Watanabe, "Line-shape analyses of solid-state ^{17}O NMR spectra for hexagonal ice," Z. Naturforsch., B **69**, 786–792 (2014).
[62]M. Adjei-Acheamfour and R. Böhmer, "Second-order quadrupole interaction based detection of ultra-slow motions: Tensor operator framework for central-transition spectroscopy and the dynamics in hexagonal ice as an experimental example," J. Magn. Reson. **249**, 141–149 (2014).
[63]L. Hoffmann, J. Beerwerth, M. Adjei-Körner, V. Fuentes-Landete, C. M. Tonauer, T. Loerting, and R. Böhmer, "Oxygen NMR of high-density and low-density amorphous ice," J. Chem. Phys. **156**, 084503 (2022).
[64]A. Abragam, *Principles of Nuclear Magnetism* (Clarendon Press, Oxford, 1961).
[65]V. K. Michaelis, E. G. Keeler, T. C. Ong, K. N. Craigen, S. Penzel, J. E. C. Wren, S. Kroeker, and R. G. Griffin, "Structural insights into bound water in crystalline amino acids: Experimental and theoretical ^{17}O NMR," J. Phys. Chem. B **119**, 8024–8036 (2015).
[66]H. W. Spiess, B. B. Garrett, R. K. Sheline, and S. W. Rabideau, "Oxygen-17 quadrupole coupling parameters for water in its various phases," J. Chem. Phys. **51**, 1201–1205 (1969).
[67]I. Hung, G. Wu, and Z. Gan, "Second-order quadrupolar line shapes under molecular dynamics: An additional transition in the extremely fast regime," Solid State Nucl. Magn. Reson. **84**, 14–19 (2017).
[68]J. Beerwerth, M. Storek, D. Greim, J. Lueg, R. Siegel, B. Cetinkaya, W. Hiller, H. Zimmermann, J. Senker, and R. Böhmer, "Two-site jumps in dimethyl sulfone studied by one- and two-dimensional ^{17}O NMR spectroscopy," J. Magn. Reson. **288**, 84–94 (2018).
[69]R. L. Vold and R. R. Vold, "Deuterium relaxation in molecular solids," in *Advances in Magnetic and Optical Resonance*, edited by W. Warren (Academic Press, San Diego, CA, 1991), pp. 85–171.
[70]L. Vugmeyster, R. Fu, and D. Ostrovsky, "^{17}O NMR relaxation measurements for investigation of molecular dynamics in static solids using sodium nitrate as a model compound," Solid State Nucl. Magn. Reson. **134**, 101976 (2024).
[71]L. Vugmeyster and D. Ostrovsky, "Deuterium rotating frame NMR relaxation measurements in the solid state under static conditions for quantification of dynamics," Chemphyschem **20**, 333–342 (2019).
[72]Y. Dai, I. Hung, Z. Gan, and G. Wu, "Extending ^{17}O transverse relaxation measurement to satellite transitions as a direct probe of molecular dynamics in solids," Solid State Nucl. Magn. Reson. **137**, 102004 (2025).
[73]R. Zhang, T. A. Cross, X. Peng, and R. Fu, "Surprising rigidity of functionally important water molecules buried in the lipid headgroup region," J. Am. Chem. Soc. **144**, 7881–7888 (2022).
[74]L. Vugmeyster, D. Ostrovsky, T. Villafranca, J. Sharp, W. Xu, A. S. Lipton, G. L. Hoatson, and R. L. Vold, "Dynamics of hydrophobic core phenylalanine residues probed by solid-state deuteron NMR," J. Phys. Chem. B **119**, 14892–14904 (2015).
[75]L. Vugmeyster, D. Ostrovsky, A. Khadjinova, J. Ellden, G. L. Hoatson, and R. L. Vold, "Slow motions in the hydrophobic core of chicken villin headpiece subdomain and their contributions to configurational entropy and heat capacity from solid-state deuteron NMR measurements," Biochemistry **50**, 10637–10646 (2011).
[76]E. L. Hahn, "Spin echoes," Phys. Rev. **80**, 580–594 (1950).
[77]F. Wang, S. K. Ramakrishna, P. Sun, and R. Fu, "Triple-pulse excitation: An efficient way for suppressing background signals and eliminating radio-frequency acoustic ringing in direct polarization NMR experiments," J. Magn. Reson. **332**, 107067 (2021).
[78]J. Haase, M. S. Conradi, C. P. Grey, and A. J. Vega, "Population transfers for NMR of quadrupolar spins in solids," J. Magn. Reson., Ser. A **109**, 90–97 (1994).
[79]R. Fu, "Efficient heteronuclear dipolar decoupling in NMR of static solid samples using phase-wiggled two-pulse phase modulation," Chem. Phys. Lett. **483**, 147–153 (2009).
[80]A. E. Bennett, C. M. Rienstra, M. Auger, K. V. Lakshmi, and R. G. Griffin, "Heteronuclear decoupling in rotating solids," J. Chem. Phys. **103**, 6951–6958 (1995).

[81] A. G. Palmer III, "NMR probes of molecular dynamics: Overview and comparison with other techniques," Annu. Rev. Biophys. Biomol. Struct. **30**, 129–155 (2001).
[82] B. M. Fung, A. K. Khitrin, and K. Ermolaev, "An improved broadband decoupling sequence for liquid crystals and solids," J. Magn. Reson. **142**, 97–101 (2000).
[83] R. L. Vold and G. L. Hoatson, "Effects of jump dynamics on solid state nuclear magnetic resonance line shapes and spin relaxation times," J. Magn. Reson. **198**, 57–72 (2009).
[84] L. Vugmeyster and D. Ostrovsky, "Static solid-state ^{2}H NMR methods in studies of protein side-chain dynamics," Prog. Nucl. Magn. Reson. Spectrosc. **101**, 1–17 (2017).
[85] C. F. F. Karney, "Quaternions in molecular modeling," J. Mol. Graphics Modell. **25**, 595–604 (2007).
[86] J. Shao, *Mathematical Statistics* (Springer, New York, 2003).
[87] J. R. C. van der Maarel, D. Lankhorst, J. de Bleijser, and J. C. Leyte, "On the single-molecule dynamics of water from proton, deuterium and oxygen-17 nuclear magnetic relaxation," Chem. Phys. Lett. **122**, 541–544 (1985).
[88] R. Ludwig, F. Weinhold, and T. C. Farrar, "Experimental and theoretical determination of the temperature dependence of deuteron and oxygen quadrupole coupling constants of liquid water," J. Chem. Phys. **103**, 6941–6950 (1995).
[89] U. Haeberlen, "High-resolution NMR in solids: Selective averaging," in *Advances in Magnetic Resonance*, edited by J. S. Waugh (Academic Press, New York, 1976).
[90] R. J. Wittebort, M. G. Usha, D. J. Ruben, D. E. Wemmer, and A. Pines, "Observation of molecular reorientation in ice by proton and deuterium magnetic resonance," J. Am. Chem. Soc. **110**, 5668–5671 (1988).
[91] N. Bjerrum, "Structure and properties of ice," Science **115**, 385–390 (1952).
[92] T. Bauer, C. Dotta, L. Balacescu, J. Gath, A. Hunkeler, A. Böckmann, and B. H. Meier, "Line-broadening in low-temperature solid-state NMR spectra of fibrils," J. Biomol. NMR **67**, 51–61 (2017).
[93] D. Eisenberg and W. Kauzmann, *The Structure and Properties of Water* (Oxford University Press, 2005).
[94] Y. Ba, J. A. Ripmeester, and C. I. Ratcliffe, "Water molecular reorientation in ice and tetrahydrofuran clathrate hydrate from lineshape analysis of ^{17}O spin-echo NMR spectra," Can. J. Chem. **89**, 1055–1064 (2011).
[95] H. M. McConnell, "Reaction rates by nuclear magnetic resonance," J. Chem. Phys. **28**, 430–431 (1958).
[96] G. Wagner, A. Demarco, and K. Wuthrich, "Dynamics of aromatic amino acids residues in globular conformation of basic pancreatic trypsin inhibitor (BPTI)," Biophys. Struct. Mech. **2**, 139–158 (1976).
[97] L. Mariño Pérez, F. S. Ielasi, L. M. Bessa, D. Maurin, J. Kragelj, M. Blackledge, N. Salvi, G. Bouvignies, A. Palencia, and M. R. Jensen, "Visualizing protein breathing motions associated with aromatic ring flipping," Nature **602**, 695–700 (2022).